universe

IMPACT FACTOR
2.6

CITESCORE
5.2

Article

Thin Accretion Disk Around Bardeen Black Hole Surrounded by Perfect Fluid Dark Matter

Dan-Dan Cui and Haiyuan Feng

Special Issue
New Progress of Black Hole Accretion Disk

Edited by
Dr. Arghajit Jana

MDPI

https://doi.org/10.3390/universe12010008

universe

Article

Thin Accretion Disk Around Bardeen Black Hole Surrounded by Perfect Fluid Dark Matter

Dan-Dan Cui and Haiyuan Feng *

School of Physics and Electronic Engineering, Shanxi Normal University, Taiyuan 030031, China; cuidandan0728@163.com
* Correspondence: 20250084@sxnu.edu.cn

Abstract

We investigate the thin accretion disk around Bardeen black hole (BH) surrounded by perfect fluid dark matter (PFDM), focusing on how the magnetic charge g and dark matter (DM) parameter b affect its radiative properties. The results show that increasing g slightly enhances the energy flux, radiation temperature, luminosity, and efficiency, while shifting the innermost stable circular orbit (r_{isco}) inward. Additionally, the influence of b is found to be dominant, making it a key parameter in distinguishing PFDM-surrounded Bardeen BH from their Schwarzschild counterparts.

Keywords: Bardeen black hole surrounded by perfect fluid dark matter; thin accretion disk

1. Introduction

Black holes (BHs) represent some of the most mysterious and extreme predictions of general relativity (GR). As the strongest gravitational sources of gravity known in the universe, they are often characterized by rapid rotation, immense density, and strong magnetic fields. These attributes make BHs unique astrophysical laboratories for probing the fundamental nature of spacetime, matter, and energy under extreme gravitational conditions. Over the past decade, a series of landmark discoveries has transformed BHs from theoretical concepts into observable cosmic realities. The first direct evidence came from the detection of gravitational waves generated by merging BHs, observed by the LIGO and Virgo Collaborations [1,2]. This achievement was followed by the historic imaging of the M87* shadow [3–6] and, more recently, that of the supermassive BH Sgr A* at the center of our galaxy [7–12], both captured by the Event Horizon Telescope (EHT) through Very Long Baseline Interferometry. Complementary evidence also arises from the observation of electromagnetic emissions from accretion disks surrounding BHs, whose spectra and luminosity profiles reveal the dynamics of matter in strong gravitational fields [13]. Together, these discoveries mark a new era in BH astrophysics. They not only provide unprecedented tests of GR in the strong-field regime but also open promising avenues to investigate potential deviations predicted by modified gravity and to understand the complex interplay between gravity, magnetism, and high-energy plasma near event horizons.

It is a established fact that BHs themselves emit no light; however, the accretion of surrounding hot and magnetized plasma gives rise to a luminous accretion disk, which serves as the dominant source of observable emission in the vicinity of the event horizon. Within this disk, heated and accelerated electrons produce strong synchrotron and inverse Compton radiation, generating broadband electromagnetic spectra that extend from radio to X-ray frequencies [14,15]. The radiative properties of the accretion flow—such as its

Academic Editor: Arghajit Jana

Received: 11 November 2025
Revised: 18 December 2025
Accepted: 25 December 2025
Published: 29 December 2025

https://doi.org/10.3390/universe12010008

temperature, density, and magnetic field structure—play a decisive role in shaping the observed brightness and morphology of BH images. In addition, in the case of rapidly rotating BHs, the extraction of rotational energy can further enhance emission through magnetohydrodynamic processes that drive powerful relativistic jets [16,17]. Consequently, the accretion disk acts as the primary radiative engine, while the jet contributes additional nonthermal emission near the polar region. Various accretion models—including spherical inflow [18,19], geometrically thin disks [20–34], and geometrically thick disks [35–38]-have been extensively analyzed to understand how different radiative and dynamical environments influence the appearance of BH shadows and the corresponding observational signatures across multiple wavelengths.

Observations of galaxy cluster dynamics have long indicated the existence of an unseen mass component in the universe. Zwicky's analysis of the Coma Cluster revealed a substantial discrepancy between the observed luminous mass and the total gravitational mass, leading to the hypothesis of an invisible component now known as dark matter (DM) [39]. Subsequent studies by Holmberg and Smith on galactic systems and the Virgo Cluster reached similar conclusions [40,41]. However, since DM does not interact with electromagnetic radiation, it neither emits, absorbs, nor reflects light, rendering direct detection impossible. Although DM has not been directly observed, multiple independent observations provide strong indirect evidence for its existence. These include the asymptotically flat rotation curves of spiral and elliptical galaxies [42], the gravitational dynamics of galaxy clusters, and the anisotropies observed in the cosmic microwave background (CMB) [43]. Therefore, investigating the nature of DM remains crucial endeavor in astrophysics. In addition to its cosmological role, DM may significantly influence the spacetime geometry and the physical properties of matter surrounding compact objects and BHs [44–50]. Recent investigations into superradiant instability and axion-like DM accretion around BHs further suggest that DM could be indirectly detected through gravitational wave emissions [51–58].

Among various DM models, the perfect fluid dark matter (PFDM) framework treats DM as a perfect fluid and has been successfully applied to explain the observed flat rotation curves of spiral galaxies [59,60]. Moreover, References [13,59] provide empirical support for the PFDM framework, linking it to observed galactic dynamics. Several spherically symmetric BH solutions surrounded by PFDM have been derived [61–63], demonstrating that PFDM can induce notable modifications to the surrounding spacetime geometry. In particular, for the Bardeen BH immersed in PFDM, both the DM component and the magnetic charge are expected to affect the properties of the accretion disk, including its radiation flux, luminosity distribution, and overall radiative efficiency. Furthermore, observational signatures of regular BHs, including their accretion properties, are currently an active area of research, especially in light of EHT observations that probe the near-horizon region [64]. By investigating the thin accretion disk in this scenario, our work aims to provide theoretical templates that can be tested against these high-precision electromagnetic observations. These results are further compared with those obtained for standard BHs in GR without DM, providing valuable insight into the interplay between DM and BH astrophysics.

This paper is organized as follows. Section 2 presents a concise overview of the Bardeen BH surrounded by PFDM. We then examine the parameter space of the magnetic charge g and DM parameter b to determine the ranges that ensure the existence of both the inner and outer horizons. In Section 3, we derives the geodesic equations in the equatorial plane and illustrates the variation of the r_{isco} with respect to these parameters. Section 4 investigates the physical properties of thin accretion disks around PFDM-surrounded Bardeen BHs, focusing on the effects of g and b on the energy flux, radiation temperature, and emission spectrum. Finally, Section 5 summarizes the main results.

2. Bardeen Black Hole Surrounded by Perfect Fluid Dark Matter

The Bardeen BH represents the regular (singularity-free) BH model within GR. Originally proposed by Bardeen in 1968, it was introduced as a theoretical counterexample to the assumption that all gravitational collapses must lead to singularities hidden by event horizons [65,66]. Later, Ayon-Beato and García reinterpreted this model as the gravitational field of a nonlinear magnetic monopole, showing that it can be derived as an exact solution of Einstein's equations coupled to nonlinear electrodynamics (NLED) [67]. This reinterpretation endowed the Bardeen model with a well-defined physical source, thereby promoting it from a phenomenological metric to a physically motivated spacetime geometry.

In the Bardeen spacetime, the metric takes the form

$$ds^2 = -\left(1 - \frac{2Mr^2}{(r^2+g^2)^{3/2}}\right)dt^2 + \left(1 - \frac{2Mr^2}{(r^2+g^2)^{3/2}}\right)^{-1} dr^2 + r^2 d\Omega^2, \tag{1}$$

where M denotes the ADM mass and g is interpreted as the magnetic monopole charge. $d\Omega^2$ stands for the standard element on the unit 2-sphere $d\Omega^2 = d\theta^2 + \sin^2(\theta)d\phi^2$. Unlike the Reissner–Nordström solution, in which the charge term behaves as $1/r^2$, the Bardeen correction term appears as $1/r^3$, ensuring that all curvature invariants (such as R, $R_{\mu\nu}R^{\mu\nu}$, and $R_{\mu\nu\alpha\beta}R^{\mu\nu\alpha\beta}$) remain finite everywhere, including at $r = 0$. Thus, this geometry avoids the formation of a curvature singularity, while still allowing for the existence of event horizons.

Physically, the regularity of the Bardeen BH originates from the coupling between gravity and a nonlinear electromagnetic field characterized by the Lagrangian $\mathcal{L}(F)$

$$\mathcal{L}(F) = \frac{3M}{|g|^3}\left(\frac{\sqrt{2g^2F}}{1+\sqrt{2g^2F}}\right)^{\frac{5}{2}}, \tag{2}$$

which satisfies the weak energy condition. where $F_{\mu\nu} = \nabla_\mu A_\nu - \nabla_\nu A_\mu$ and $\mathcal{L}(F)$ is a function of $\frac{1}{4}F_{\mu\nu}F^{\mu\nu}$. In a broader astrophysical setting, incorporating PFDM into the Bardeen spacetime provides a natural framework for studying the interplay between DM and regular BHs. Since PFDM effectively captures the large-scale DM distribution that influences galactic dynamics and BH environments, embedding it within the Bardeen geometry enables a detailed examination of how DM affects the horizon structure, thermodynamic properties, and energy conditions of a regular BH. Assuming that the BH is immersed in a PFDM background, Zhang et al. [68] further investigated the coupling between gravity and a nonlinear electromagnetic field, and derived the corresponding Bardeen BH surrounded by PFDM. The energy–momentum tensor can be written as

$$T^\mu_\nu = \mathrm{diag}(-\rho, p_r, p_\theta, p_\phi), \tag{3}$$

with

$$\rho = -p_r = \frac{b}{r^3}, \quad p_\theta = p_\phi = \frac{b}{2r^3}, \tag{4}$$

where ρ, p_r, and $p_\theta = p_\phi$ denote the energy density, radial pressure, and tangential pressures of the DM, respectively [69]. The weak energy condition $T_{tt} \geq 0$ outside the event horizon imposes the constraint $b \geq 0$ [68]. In this framework, attention is mainly directed toward the localized effects of DM in the vicinity of the BH, rather than its global cosmological influence on the asymptotic properties. As a result, the DM parameter b reflects the local density profile and dynamical interaction of DM surrounding the BH, and is not associated with large-scale cosmological quantities such as the overall DM content of the universe. In observational contexts, b can be constrained by comparing model-based predictions—for instance, from galaxy rotation dynamics or angular diameter of the BH shadow-with empirical data obtained for particular BH systems.

Furthermore, considering that the metric is static and spherically symmetric, the corresponding BH solution can be expressed in the following form

$$ds^2 = -f(r)dt^2 + f(r)^{-1}dr^2 + r^2 d\Omega^2, \tag{5}$$

and

$$f(r) = 1 - \frac{2Mr^2}{(r^2+g^2)^{\frac{3}{2}}} - \frac{b}{r}\ln\frac{r}{|b|}. \tag{6}$$

From the above equation, it is evident that the solution reduces to the Schwarzschild BH when both the DM parameter $b = 0$ and the magnetic charge $g = 0$. In the absence of DM, the spacetime corresponds to the Bardeen BH, while setting $g = 0$ yields the Schwarzschild BH surrounded by PFDM. In Figure 1, we plot the inner and outer horizons of the Bardeen BH, the Schwarzschild BH surrounded by PFDM, and the Bardeen BH immersed in PFDM. The horizontal axis represents the dimensionless radial coordinate r/M, while the vertical axis denotes the metric function $f(r)$. The condition $f(r) = 0$ determines the locations of the inner and outer horizons.

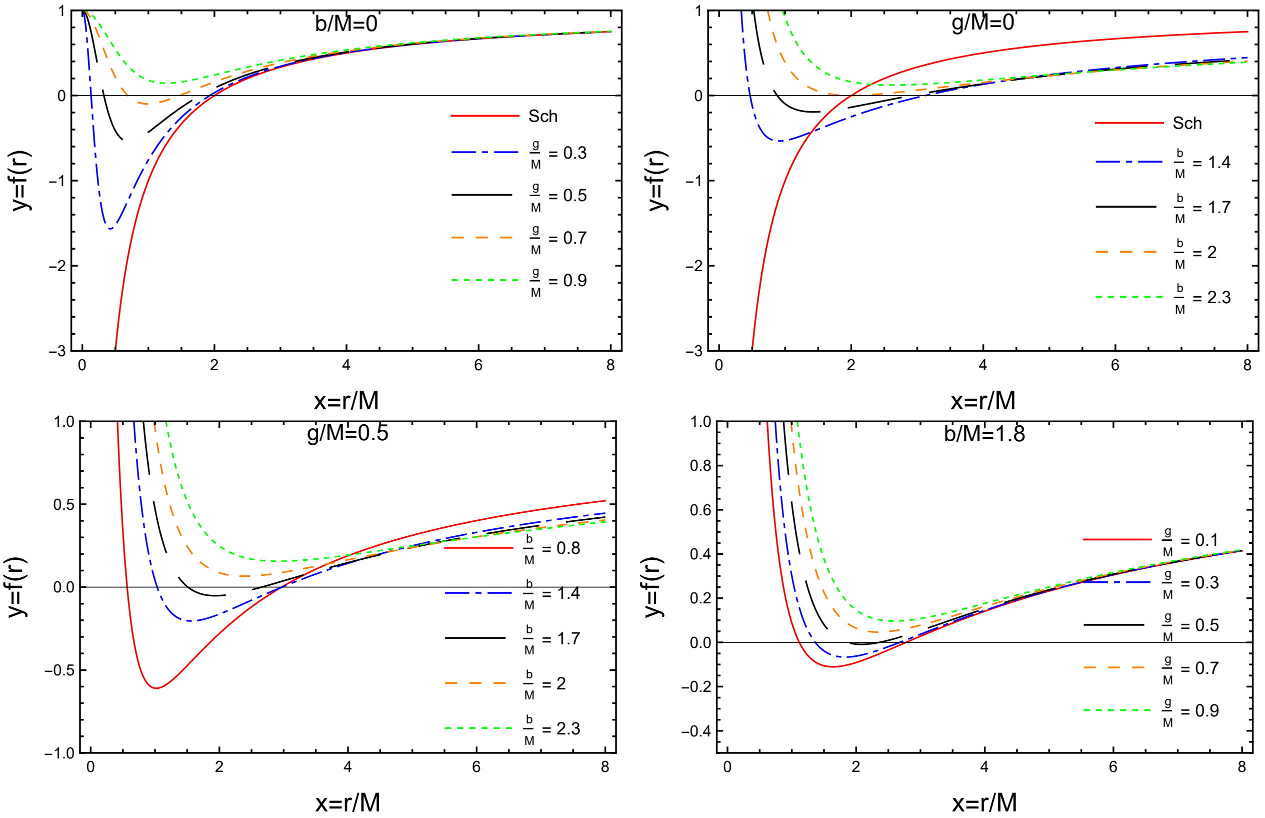

Figure 1. The upper-left panel corresponds to the Bardeen BH compared with the Schwarzschild case, the upper-right panel shows the Schwarzschild BH surrounded by PFDM, and the lower panel illustrates the Bardeen BH immersed in PFDM.

From the Bardeen BH, it can be seen that the Schwarzschild BH possesses only a single event horizon, whereas the presence of a magnetic charge g introduces two horizons until a critical configuration is reached, corresponding to an extremal BH. By solving $f(r_*, g) = 0$ and $f'(r_*, g) = 0$, the maximum magnetic charge is found to be $g/M = 0.7698$, with the coincident horizons located at $r_+/M = r_-/M = r_*/M = 1.08866$. This implies that two horizons exist for $g/M \in (0, 0.7698)$, while no horizon appears beyond this range. For the second type of BH—the Schwarzschild BH surrounded by PFDM—a similar analysis shows that the dark matter parameter b/M admits two horizons only within the interval $b/M \in (0, 2)$; outside this range, the spacetime represents a naked singularity. Finally, the third type—the Bardeen BH immersed in PFDM—is illustrated in the bottom panels of Figure 1. In this case, the extremal BH condition is determined by the system of equations $f(r_*, g, b) = 0$ and $f'(r_*, g, b) = 0$. These equations define a curve in the two-dimensional (b, g) parameter space, which separates the BH region from the naked singularity region. The values of b/M selected in this study are intended to comprehensively illustrate the effects of PFDM across the theoretical parameter space. In realistic astrophysical scenarios, the value of b should be constrained by observations. For instance, for the Galactic center BH Sgr A*, observational constraints on the enclosed DM mass within the central parsec-derived from stellar dynamics and preliminary shadow analyses-imply an upper limit on the DM density [70]. However, we restrict our parameter space to only include those values where the BH possesses both an inner and an outer horizon. We do not impose constraints on the parameters based on known astrophysical BHs. Furthermore, utilizing a larger value of b allows for a better distinction between our model's predictions and those of GR.

3. Timelike Geodesics Equations and Stable Circular Orbits

In this section, we investigate the timelike geodesics and the conditions for stable circular orbits around the Bardeen BH immersed in PFDM. The motion of a massive test particle follows the timelike geodesics determined by the underlying spacetime geometry, which provides important insights into the gravitational structure and accretion disk dynamics. By analyzing the effective potential associated with the particle's motion, one can identify the regions where circular orbits are allowed and determine their stability criteria.

The formation of an accretion disk originates from the motion of particles that follow geodesic trajectories around a compact central object under the influence of gravity. These particles gradually lose angular momentum through various dissipative processes, allowing them to settle into nearly circular orbits and form a geometrically thin, optically thick disk structure. The motion of the particles, and consequently the overall dynamics of the accretion disk, are entirely determined by the background spacetime geometry. In the case of a static and spherically symmetric spacetime, the metric that governs such motion can be expressed in the following general form

$$\mathrm{d}s^2 = g_{tt}\,\mathrm{d}t^2 + g_{rr}\,\mathrm{d}r^2 + g_{\theta\theta}\mathrm{d}\theta^2 + g_{\phi\phi}\mathrm{d}\phi^2, \tag{7}$$

where the metric given in Equation (7), owing to the symmetry of the spacetime-namely, the existence of a timelike Killing vector field $\frac{\partial}{\partial t}$ associated with time-translation invariance and three spacelike Killing vector fields corresponding to rotational symmetry on the two-sphere (S^2)—the metric components g_{tt}, g_{rr}, $g_{\theta\theta}$, and $g_{\phi\phi}$ depend solely on the radial coordinate r. In this study, we focus on the motion of test particles confined to the equatorial plane $(\theta = \pi/2)$. Within this spacetime geometry, two conserved quantities naturally emerge: the specific energy at infinity, denoted by $\tilde{E}$, and the z-component of the specific angular momentum at infinity, denoted by $\tilde{L}$ [71]. These quantities arise directly from the spacetime's Killing symmetries associated with time translation and axial rotation. These quantities can be given by

$$\begin{cases} g_{tt}\frac{\mathrm{d}t}{\mathrm{d}\tau} = -\tilde{E}, \\ g_{\phi\phi}\frac{\mathrm{d}\phi}{\mathrm{d}\tau} = \tilde{L}, \end{cases} \tag{8}$$

here τ denotes the affine parameter along the particle's worldline. In the equatorial plane, the timelike geodesic equation governing the motion of a massive test particle can be derived from the metric through the Euler-Lagrange formalism. By exploiting the symmetries of BH, one obtains a simplified form of the geodesic equation

$$\begin{cases} \frac{\mathrm{d}t}{\mathrm{d}\tau} = -\frac{\tilde{E}}{g_{tt}}, \\ \frac{\mathrm{d}\phi}{\mathrm{d}\tau} = \frac{\tilde{L}}{g_{\phi\phi}}, \\ g_{rr}\left(\frac{\mathrm{d}r}{\mathrm{d}\tau}\right)^2 = V_{\mathrm{eff}}(r), \end{cases} \tag{9}$$

with the effective potential

$$V_{\mathrm{eff}} = -\frac{\tilde{E}^2 g_{\phi\phi} + \tilde{L}^2 g_{tt}}{g_{tt}g_{\phi\phi}} - 1. \tag{10}$$

For a particle to maintain circular orbit in the equatorial plane, the following conditions must be simultaneously satisfied [72–74]

$$V_{\mathrm{eff}} = 0, \quad \frac{\partial V_{\mathrm{eff}}}{\partial r} = 0. \tag{11}$$

Because the spacetime exhibits reflection symmetry about the equatorial plane, particles located at $\theta = \pi/2$ naturally satisfy the condition $\partial_\theta V_{\mathrm{eff}} = 0$. Under these equilibrium conditions, the motion of test particles becomes purely circular and stable within the equatorial plane. By applying the above relations, one can derive explicit expressions for the specific energy $\tilde{E}$, specific angular momentum $\tilde{L}$, and specific angular velocity Ω, which follows

$$\begin{cases} \tilde{E} = \frac{-g_{tt}}{\sqrt{-g_{tt}-\Omega^2 g_{\phi\phi}}} = \frac{\sqrt{2}\left(g^2 r\sqrt{g^2+r^2}+r^3\left(-2+\sqrt{g^2+r^2}\right)-b\left(g^2+r^2\right)^{3/2}\ln\left(\frac{r}{b}\right)\right)}{\left(g^2+r^2\right)^{3/2}\sqrt{br+2r^2-\frac{6r^6}{\left(g^2+r^2\right)^{5/2}-3b\ln\left(\frac{r}{b}\right)}}}, \\ \tilde{L} = \frac{\Omega g_{\phi\phi}}{\sqrt{-g_{tt}-\Omega^2 g_{\phi\phi}}} = \frac{r\sqrt{b\ln\left(\frac{r}{b}\right)-b+\frac{2\left(r^5-2g^2r^3\right)}{\left(g^2+r^2\right)^{5/2}}}}{\sqrt{-3b\ln\left(\frac{r}{b}\right)+b-\frac{6r^5}{\left(g^2+r^2\right)^{5/2}}+2r}}, \end{cases} \tag{12}$$

where the angular velocity is

$$\Omega = \frac{\mathrm{d}\phi}{\mathrm{d}t} = \pm\frac{\sqrt{-g_{tt,r}g_{\phi\phi,r}}}{g_{\phi\phi,r}} = \pm\sqrt{\frac{b\ln\left(\frac{r}{b}\right) - b + \frac{2\left(r^5-2g^2r^3\right)}{\left(g^2+r^2\right)^{5/2}}}{2r^3}}. \tag{13}$$

It should be emphasized that the positive and negative signs in the derived expressions represent the co-rotating (prograde) and counter-rotating (retrograde) motions of test particles, respectively, relative to the rotation direction of the BH.

For test particles orbiting the Bardeen BH surrounded by PFDM, the innermost stable circular orbit (ISCO) is defined as the radius where the second derivative of the effective potential with respect to the radial coordinate vanishes, $V_{\mathrm{eff},rr} = 0$. This condition characterizes the marginally stable orbit, marking the transition between stable and unstable circular motion. Additionally, the effective potential can be expressed as

$$V_{\mathrm{eff}} = -1 + \frac{f_1}{f_2}, \tag{14}$$

where $f_1 = \tilde{E}^2 g_{\phi\phi} + \tilde{L}^2 g_{tt}$ and $f_2 = -g_{tt}g_{\phi\phi}$, with the constraint $f_2 \neq 0$ to maintain regularity. By imposing the circular orbit condition $V_{\mathrm{eff}}(r) = 0$, one obtains the relation $f_1 = f_2$. Differentiating with respect to r and applying $V_{\mathrm{eff},r}(r) = 0$ yields $f_{1,r}f_2 - f_1 f_{2,r} = 0$.

Combining these relations and further requiring $V_{\mathrm{eff},rr}(r) = 0$ provides the critical condition that determines the ridus of ISCO (r_{isco})

$$0 = (-g_{tt}g_{\phi\phi})V_{\mathrm{eff},rr} = \tilde{E}^2 g_{\phi\phi,rr} + \tilde{L}^2 g_{tt,rr} - (-g_{tt}g_{\phi\phi})_{,rr}, \tag{15}$$

beyond which circular orbits become dynamically unstable. It is noteworthy that the r_{isco} can also be derived using an alternative method, referred to here as method $\frac{d\tilde{E}}{dr} = 0$. These two approaches are analytically equivalent, and after extensive algebraic manipulation, the governing equation for determining r_{isco} can be written as

$$\begin{aligned}
&4\Big[8g^6r^4\sqrt{g^2+r^2} - 9g^2r^8\sqrt{g^2+r^2} + b^2\left(g^2+r^2\right)^5 \\
&-4br^3\sqrt{g^2+r^2}\left(-2g^6-3g^4r^2+r^6\right) - r^{10}\left(-6+\sqrt{g^2+r^2}\right)\Big] \\
&+2b\left(g^2+r^2\right)\ln\left(\frac{r}{b}\right)\Big[-30g^4r^3\sqrt{g^2+r^2} + 12g^2r^5\sqrt{g^2+r^2} + \\
&12r^7\sqrt{g^2+r^2} - 4b\left(g^2+r^2\right)^4 - r\left(g^2+r^2\right)^4 + 3b\left(g^2+r^2\right)^4\ln\left(\frac{r}{b}\right)\Big] = 0.
\end{aligned} \tag{16}$$

Given that the resulting analytical expression for the ISCO radius is intractable, its functional dependence on the governing parameter was subsequently determined and plotted using numerical root-finding algorithm implemented in Mathematica.In Figure 2, we present the variations of the r_{isco} as functions of the magnetic charge g, and the DM parameter b.

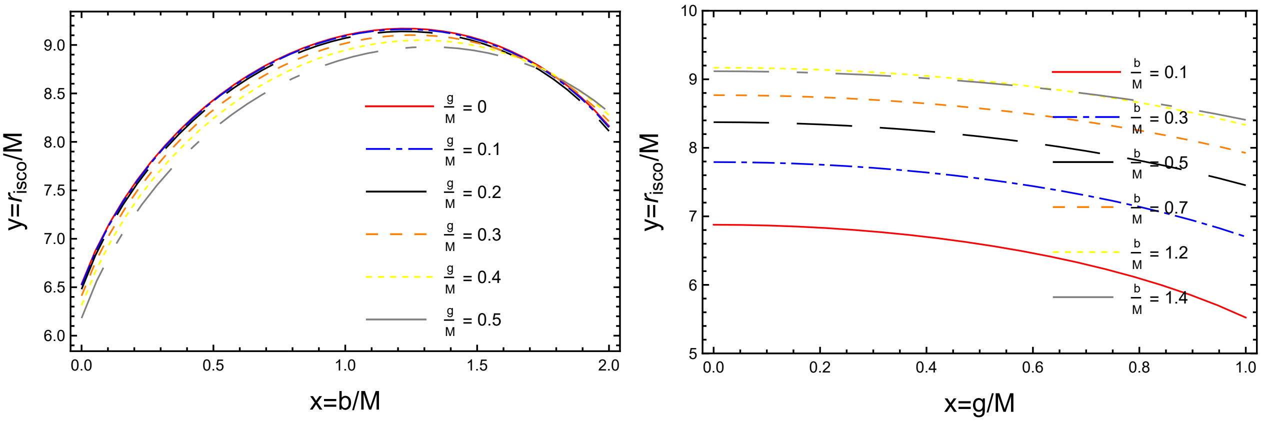

Figure 2. These two panels illustrate the dependence of the r_{isco} on the the DM parameter b and magnetic charge g, respectively.

From the left panel of Figure 2, it is evident that r_{isco} varies differently with the DM parameter b. The red curve represents Schwarzschild BH surrounded by PFDM. As the magnetic charge g increases, r_{isco} for the PFDM surrounded BH decreases relative to the Schwarzschild case, indicating that larger g reduces the radius. Likewise, the right panel of Figure 2 shows that, for a fixed b, increasing g decreases r_{isco}. In contrast, the right panel of Figure 2 reveals a non-monotonic relationship: for a fixed magnetic charge g, as the DM parameter b increases, r_{isco} initially expands before eventually decreasing.

This phenomenon stems from the fact that PFDM modifies the spacetime geometry by introducing a non-zero energy momentum tensor. Specifically, the logarithmic term in the metric potential $f(r)$ alters the radial dependence of the metric (Figure 1), which in turn modifies the Riemann curvature components in the vicinity of the r_{isco}. According to the Ricci scalar $R = \frac{6Mg^2(4g^2-r^2)}{(g^2+r^2)^{7/2}} + \frac{b}{r^3}$, a clear competition arises between the Bardeen term

$\left(\frac{6Mg^2(4g^2-r^2)}{(g^2+r^2)^{7/2}}\right)$ and the PFDM contribution $\left(\frac{b}{r^3}\right)$. For Schwarzschild BH surrounded by PFDM ($g = 0$), the Ricci scalar remains strictly positive due to the dominance of the second term. However, for Bardeen BH surrounded by PFDM, the first term typically yields a negative value at (r_{isco}). The inclusion of the PFDM parameter b acts to counteract this negativity, effectively shifting the curvature from negative to positive values. Consequently, the Ricci curvature of Bardeen BH surrounded by PFDM exhibits a unique transition, characterized by being initially lower than that of Schwarzschild case before surpassing it as the influence of DM parameter b prevails.

4. Continuum Spectrum in Bardeen Black Hole Surrounded by Perfect Fluid Dark Matter

Thin accretion disk surrounding BH is a rotating structure formed by infalling matter under strong gravitational attraction. Governed by gravity, magnetic fields, and viscous effects, it constitutes one of the most dynamic regions near a BH. The disk, composed of rapidly orbiting rings, emits intense radiation—from optical to X-rays and gamma rays—due to energy dissipation in its plasma. The temperature increases toward the inner regions, producing complex spectral features. Investigating thin accretion disks is crucial for understanding accretion dynamics and high-energy astrophysical phenomena.

In this section, we will investigate the radiant energy flux, radiation temperature, and observed luminosity from thin accretion disk. These calculations are used to investigate observable characteristics of Bardeen BH surrounded by PFDM and to identify potential diagnostics for distinguishing it from the GR BHs. The continuum spectrum is modeled within the Novikov–Thorne framework [75,76], which relies on the following key assumptions:

(1) The system is in a steady state with a constant mass accretion rate throughout the disk.
(2) The accreting matter follows nearly Keplerian motion, implying the absence of a significant large-scale magnetic field.
(3) The disk is geometrically thin, with a vertical scale much smaller than its radial extent, allowing efficient radiative cooling of viscously generated energy.
(4) The disk radiates locally as a black body in thermal equilibrium, emitting perpendicularly to the disk plane, consistent with an optically thick medium.
(5) The continuum spectrum is dominated by thermal emission from the accretion disk.
(6) The background spacetime is stationary, axisymmetric, and asymptotically flat, with reflection symmetry across the equatorial plane.
(7) The self-gravity of the disk is negligible and does not alter the background metric.
(8) Gas particles orbit between the innermost stable circular orbit (r_{isco}), and an outer radius r_{out}.
(9) The disk lies in the equatorial plane, aligned with the black hole's spin axis.

Although the Novikov–Thorne model has been previously applied to various BHs, we revisit its formulation here in spherical coordinates—an approach not frequently used in earlier studies—to systematically investigate the radiation properties around Bardeen BH in a PFDM environment.

Furthermore, the study of accretion disk radiation requires a set of fundamental physical parameters. In the following analysis, we adopt the following values for the physical constants and thin accretion disk parameters: $c = 2.997 \times 10^{10}$ cm s^{-1}, $M_\odot = 1.989 \times 10^{33}$ g, $\dot{M}_0 = 2 \times 10^{-6}\ M_\odot$ yr^{-1}, 1 yr $= 3.156 \times 10^7$ s, $\sigma_{\text{SB}} = 5.67 \times 10^{-5}$ erg s^{-1} cm^{-2} K^{-4}, $h = 6.625 \times 10^{-27}$ ergs, and $k_{\text{B}} = 1.38 \times 10^{-16}$ erg K^{-1}. The BH mass is set to $M = 2 \times 10^6\ M_\odot$. The supermassive BH SgrA* at the Galactic center serves as an astrophysical example of such a system, with a mass of approximately $4.1 \times 10^6\ M_\odot$ and an estimated accretion rate in the range $\dot{M}_0 = 10^{-9} - 10^{-7}\ M_\odot\ \mathrm{yr}^{-1}$.

It is worth emphasizing that we adopt the Novikov–Thorne model as a geometric probe to examine how the spacetime of PFDM-surrounded Bardeen BH affects radiative properties. The Novikov–Thorne framework is analytically tractable, enabling energy flux and luminosity to be computed directly from the background metric. This transparency allows the effects of the DM parameter (b) and magnetic charge (g) to be isolated without the complexities and physical degeneracies inherent in thick-disk GRMHD simulations. We emphasize that the EHT parameters used in our analysis, such as the BH mass and accretion rate, serve only as astrophysical scale inputs and do not imply an assumption that the actual accretion flows in Sgr A* or M87* are thin or cold. Instead, our results will provide a theoretical baseline that highlights the fundamental geometric influence of DM, with the identified qualitative trends expected to remain robust in more complex, geometrically thick accretion scenarios.

4.1. The Radiant Energy Flux

In the steady-state accretion disk model, the infalling matter is described as an anisotropic fluid, whose dynamics are governed by the energy–momentum tensor [77,78].

$$T_{\mu\nu} = \epsilon_0 u_\mu u_\nu + 2u_{(\mu}q_{\nu)} + t_{\mu\nu}, \tag{17}$$

here, ϵ_0, q_μ, and $t_{\mu\nu}$ denote the rest-mass density, energy flux vector, and stress tensor, respectively. These quantities are defined in the averaged rest frame of the orbiting fluid elements with four-velocity u_μ, where q_μ and $t_{\mu\nu}$ are orthogonal to u_μ ($u^\mu q_\mu = 0$ and $u^\mu t_{\mu\nu} = 0$). This tensor formulation effectively captures the transport of energy, angular momentum, and radiation within the disk, allowing one to characterize the physical processes underlying viscous dissipation, thermal emission, and mass accretion in the vicinity of the BH. Additionally, in the steady-state regime, the particle motion is assumed to follow nearly geodesic orbits, implying that the gravitational attraction of the central BH overwhelmingly dominates over the pressure gradients. Consequently, the specific internal energy of the accreting fluid is negligible compared to its rest-mass energy.

To evaluate the flux and luminosity emitted from the accretion disk, the Novikov–Thorne model assumes that the accreting fluid obeys the conservation laws of mass, energy, and angular momentum, expressed as

$$\begin{cases} \dot{M} = -2\pi\sqrt{-\tilde{g}}\Sigma(r)u^r = \mathrm{const} \\ \left(\dot{M}\tilde{E} - 2\pi\sqrt{-\tilde{g}}\Omega W^r_\phi\right)_{,r} = 2\pi\sqrt{-\tilde{g}}F(r)\tilde{E} \\ \left(\dot{M}\tilde{L} - 2\pi\sqrt{-\tilde{g}}W^r_\phi\right)_{,r} = 2\pi\sqrt{-\tilde{g}}F(r)\tilde{L}, \end{cases} \tag{18}$$

where $\Sigma(r) = \int_{-H}^{H}\langle\epsilon_0\rangle dz$ and $W^r_\phi = \int_{-H}^{H}\langle t^r_\phi\rangle dz$ are the averaged rest mass density and the averaged stress tensor, respectively. $\tilde{g}$ denotes the determinant of the near-equatorial metric in cylindrical coordinates, and $\langle t^r_\phi\rangle$ represents the time-averaged value of the stress tensor. By employing the energy–angular momentum relation for circular geodesic orbits, $\tilde{E}_{,r} = \Omega\tilde{L}_{,r}$, the term W^r_ϕ in Equation (18) can be eliminated, leading to the final expression for the radiative energy flux.

$$F(r) = -\frac{\dot{M}}{4\pi\sqrt{-\tilde{g}}}\frac{\Omega_{,r}}{(\tilde{E} - \Omega\tilde{L})^2}\int_{r_{\mathrm{isco}}}^{r}(\tilde{E} - \Omega\tilde{L})\tilde{L}_{,r}\,\mathrm{d}r. \tag{19}$$

This equation has been widely used in the literature and is valid only in cylindrical coordinates. When expressed in spherical coordinates with restored physical dimensions, it takes the following form [79]

$$F(r) = -\frac{c^2 \dot{M}}{4\pi\sqrt{-g/g}} \frac{\Omega_{,r}}{(\tilde{E} - \Omega\tilde{L})^2} \int_{r_{\rm isco}}^{r} (\tilde{E} - \Omega\tilde{L})\tilde{L}_{,r}\, \mathrm{d}r, \tag{20}$$

here, c denotes the speed of light. We consider mass accretion onto BH with total mass $M = 2 \times 10^6\ M_\odot$ and corresponding accretion rate $\dot{M}_0 = 2 \times 10^{-6}\ M_\odot\ \mathrm{yr}^{-1}$.

The Figure 3 presents the variation of the radiative energy flux $F(r)$ with radial distance. For fixed magnetic charge values of $g/M = 0, 0.1, 0.3, 0.5$, the profiles exhibit a Planck distribution, where the peak shifts toward larger radii as the DM parameter increases. The flux magnitude remains on the order of 10^{13} erg. Moreover, increasing b alters the location of the $r_{\rm isco}$, which serves as the starting point for our numerical analysis.

Subsequently, the Figure 4 shows the effect of the magnetic charge g on the radiative energy flux for fixed values of the DM parameter b. The variation of the flux with respect to g is relatively weak; however, a slight enhancement in the flux is observed as g increases. The peak gradually shifts toward smaller radii and becomes more pronounced with increasing g. Moreover, the radiative flux of the Bardeen BH surrounded by PFDM is consistently higher than that of the Schwarzschild BH in the same environment.

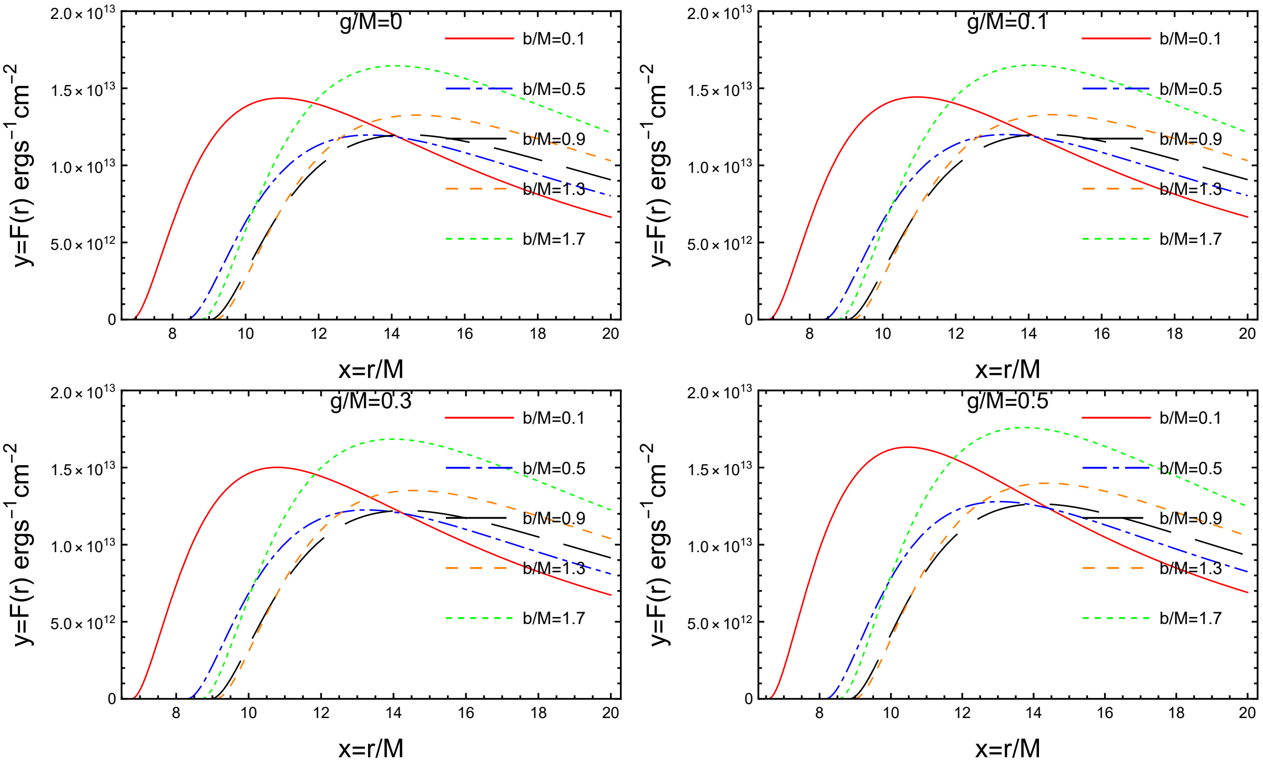

Figure 3. The energy flux $F(r)$ of the accretion disk is analyzed for magnetic charge values $g/M = 0, 0.1, 0.3, 0.5$ under different DM parameter b settings.

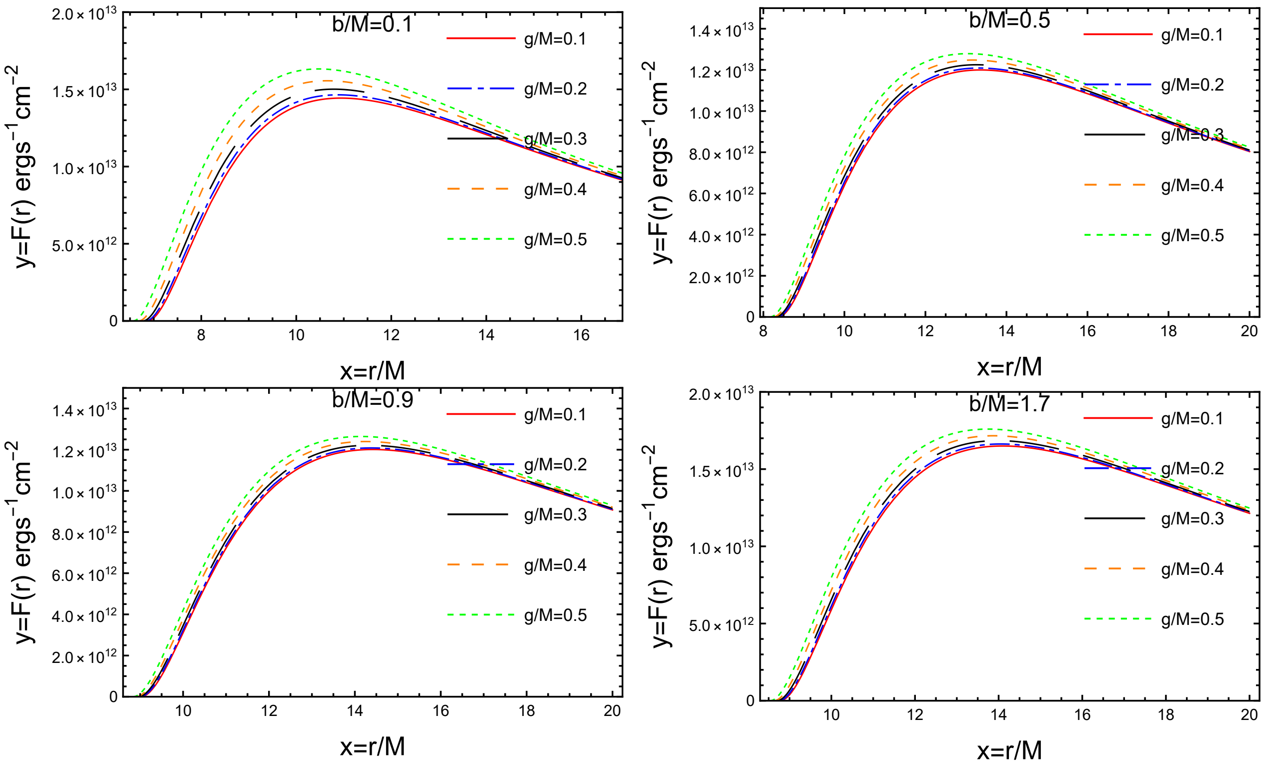

Figure 4. The energy flux $F(r)$ of the accretion disk is analyzed for DM parameter $b/M = 0.1, 0.5, 0.9, 1.7$ under different magnetic charge g settings.

4.2. The Radiation Temperature

We now investigate the radial distribution of the disk radiation temperature $T(r)$. In the framework of the steady-state thin disk model, the accreting matter is assumed to maintain local thermal equilibrium, such that the energy generated through viscous dissipation is efficiently radiated away from the disk surface. Consequently, the emitted radiation can be well approximated by that of a perfect blackbody. Under this assumption, the local temperature $T(r)$ is directly related to the energy flux $F(r)$ through the Stefan–Boltzmann law,

$$F(r) = \sigma_{\rm SB} T^4(r), \tag{21}$$

where $\sigma_{\rm SB}$ is the Stefan–Boltzmann constant. This relation provides a direct means to connect the thermodynamic properties of the accreting matter with the observable radiation characteristics of the disk.

Based on Figure 5, the radiation temperature $T(r)$ of the accretion disk exhibits clear dependence on both the magnetic charge g and DM parameter b. For each fixed magnetic charge, the temperature profile maintains a characteristic peak, whose position and magnitude vary with b. As b increases, the peak of $T(r)$ shifts outward.

Figure 6 illustrates the variation of the radiation temperature $T(r)$ for fixed b and different g. The profiles exhibit similar qualitative behavior across all cases, showing a rapid rise near the inner edge of the disk, followed by a gradual decline at larger radii. As the magnetic charge increases, the peak temperature shifts slightly toward smaller radii and becomes marginally higher, indicating that the magnetic charge has a mild but noticeable effect on the thermal properties of the accretion disk. It is also evident that the radiation temperature exhibits behavior similar to that of the radiative energy flux. The Bardeen BH surrounded by PFDM shows a higher radiation temperature compared with the Schwarzschild BH in the same environment, with the temperature magnitude on the order of 10^3 K.

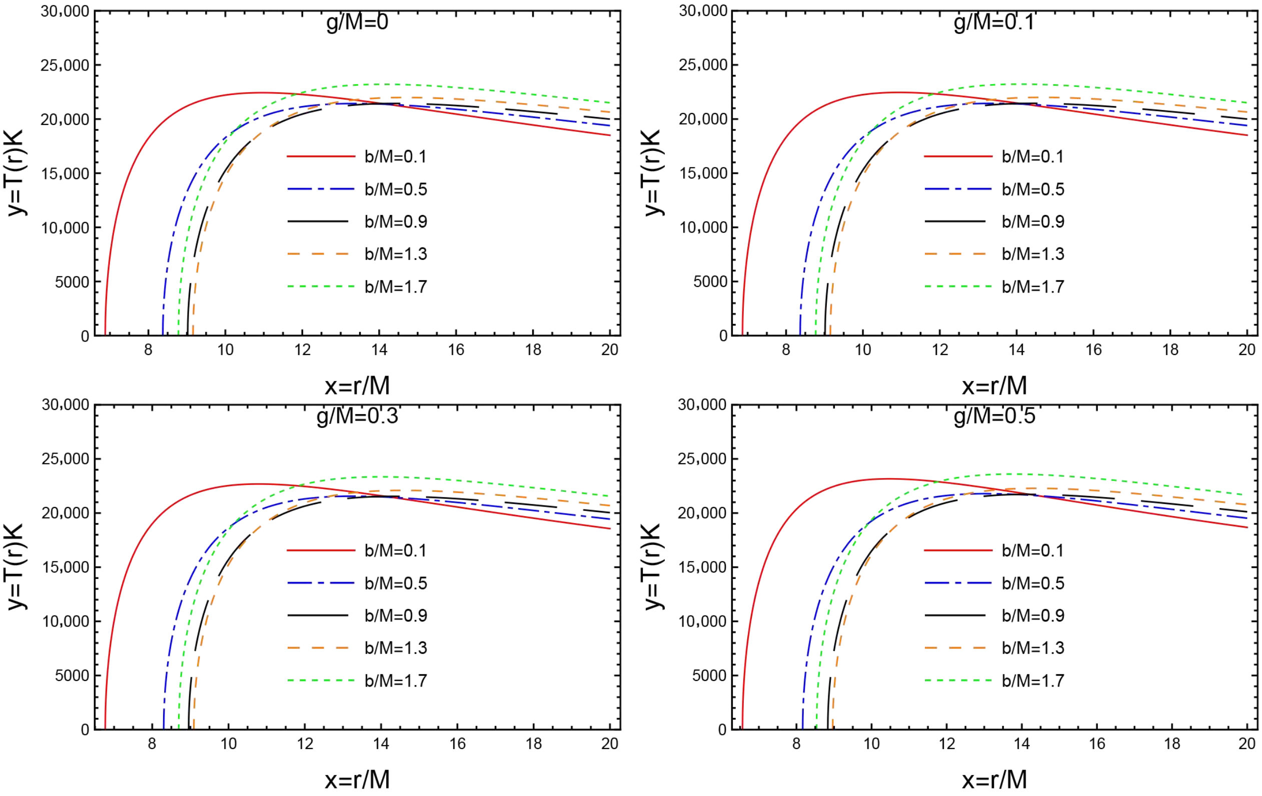

Figure 5. The radiation temperature profiles are examined for fixed g under different b.

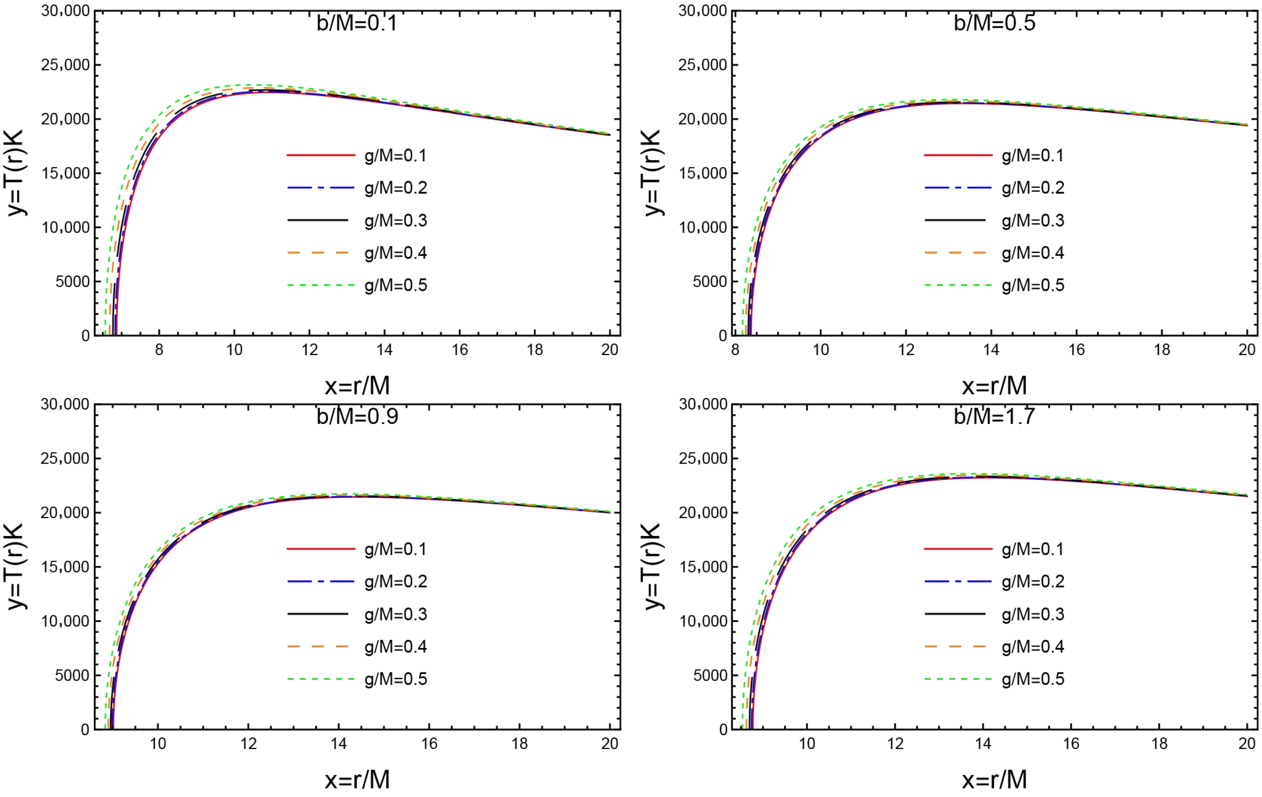

Figure 6. The radiation temperature profiles are analyzed for fixed b with varying g.

4.3. The Observed Luminosity

The observed luminosity is key diagnostic quantities in characterizing the accretion process around compact objects. The luminosity $L(\nu)$ represents the total radiative power received by a distant observer per unit frequency, accounting for the redshift of photons as they propagate from the emitting surface of the disk to infinity [80,81]. In relativistic disk models, the observed luminosity incorporates both gravitational redshift arising from the orbital motion of the emitting material. Accordingly, the luminosity can be expressed as

$$L(v) = 4\pi\, \mathrm{d}^2 I(v) = \frac{8\pi h \cos\gamma}{c^2} \int_{r_\mathrm{i}}^{r_\mathrm{f}} \int_0^{2\pi} \frac{v_\mathrm{e}^3 r \,\mathrm{d}\phi\, \mathrm{d}r}{e^{\frac{h v_\mathrm{e}}{k_\mathrm{B} T}} - 1}, \tag{22}$$

where d denotes the distance from the center of the accretion disk, $I(\nu)$ represents the specific intensity of the radiation emitted from the disk surface, h is the Planck constant, k_B is the Boltzmann constant, and γ is the inclination angle of the disk, for which we take $\gamma = 0$ corresponding to a face-on observer. The quantities r_i and r_f refer to the inner and outer edges of the disk, respectively. Following the standard thin-disk assumption, the radiation flux gradually vanishes at large radii, thus we adopt $r_\mathrm{i} = r_\mathrm{isco}$ and $r_\mathrm{f} \to \infty$.

In addition, the emitted frequency is related to the observed frequency through the redshift relation $\nu_\mathrm{e} = \nu(1+z)$, where z represents the total redshift experienced by photons as they travel from the disk to the observer. This redshift factor encapsulates both gravitational contributions arising from the curved spacetime geometry and the orbital motion of the emitting material, and it can be expressed as

$$1 + z = \frac{1 + \Omega r \sin\phi \sin\gamma}{\sqrt{-g_{tt} - 2\Omega g_{t\phi} - \Omega^2 g_{\phi\phi}}}, \tag{23}$$

where the bending effect of light has been ignored [82,83]. While our model employs certain simplifications, accounting for these factors would primarily yield quantitative refinements without altering the core qualitative conclusions. Specifically, incorporating gravitational lensing would enhance the absolute observed flux through multiple imaging of the disk's far side, yet the spectral peak position—dictated by the intrinsic energy distribution—remains largely stable. Similarly, non-zero inclination angle would introduce Doppler-induced asymmetries, but this acts as a secondary modulation that does not counteract the fundamental peak shifts driven by the parameter b. Furthermore, although BH spin typically reduces r_isco, its influence is distinct from the PFDM-induced modifications to the gravitational potential. In rotating system, the competing effects of spin and DM would coexist, but for fixed spin, the characteristic trend of r_isco varying with b would still persist, even if the absolute radii are smaller. Consequently, although accounting for these effects might lead to slight numerical variations, the core qualitative findings are unaffected. This demonstrates that our current simplifications are both reasonable.

Figure 7 shows the variation of the disk luminosity $\nu L(\nu)$ with frequency ν for the Bardeen BH surrounded by PFDM at different values of b. From the plots, it is evident that for a given magnetic charge g, the spectral luminosity increases with the DM parameter b. Specifically, both the peak value and the total luminosity of the emission spectrum rise as b increases. This behavior indicates that the presence of PFDM enhances the radiative luminosity of the accretion disk, leading to stronger emission. Physically, this can be attributed to the modification of the spacetime geometry by the DM component, which affects the effective potential and consequently the energy release rate in the disk.

Figure 8 illustrates the effect of the magnetic charge g on the radiative luminosity for a fixed value of the DM parameter b. It is evident that the variation of g produces only a marginal influence on the disk luminosity, with a slight increase in g leading to a minor enhancement in the overall emission intensity. This indicates that the magnetic charge contributes weakly to the accretion efficiency and thermal emission of the disk. Moreover, the luminosity profiles of the Bardeen BH surrounded by PFDM closely resemble those of the Schwarzschild BH embedded in the same DM environment, suggesting that their radiative characteristics are nearly indistinguishable. Hence, the DM parameter becomes the dominant factor in modifying the disk radiation and spectral distribution. Consequently, constraining b through high-resolution observations, such as those from the EHT, could offer a promising approach to distinguish between Bardeen and Schwarzschild BHs surrounded by PFDM.

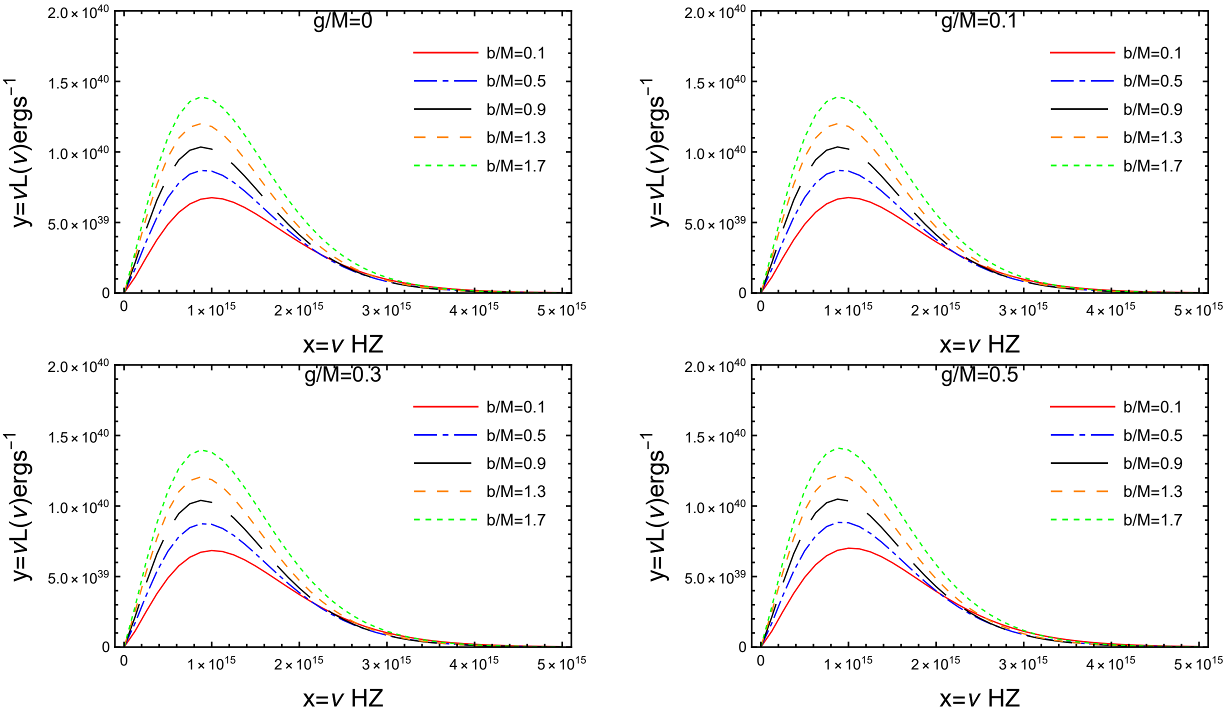

Figure 7. The emission spectrum $\nu L(\nu)$ of disk around ardeen BH surrounded by PFDM with different values of b.

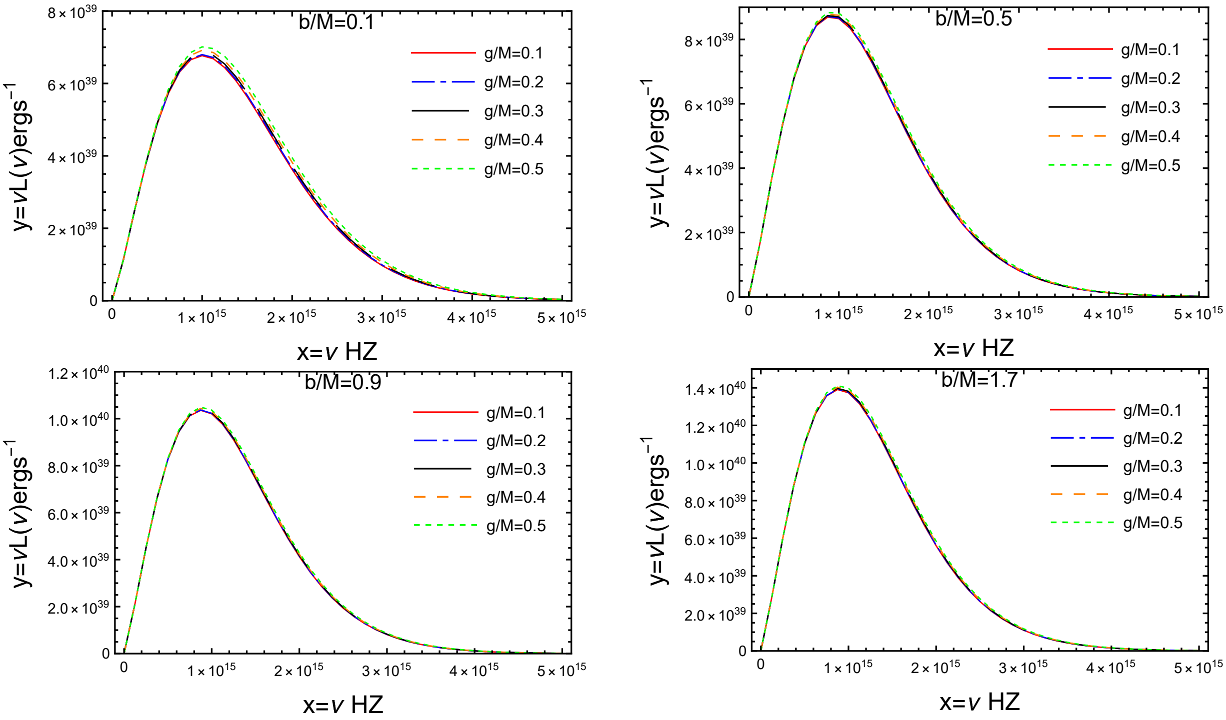

Figure 8. The emission spectrum $\nu L(\nu)$ of disk around Bardeen BH surrounded by PFDM with different values of g.

4.4. The Radiative Efficiency

The radiative efficiency ϵ of BH quantifies the fraction of the rest-mass energy of the accreting material that is transformed into radiation during the accretion process. It serves as a fundamental parameter governing the overall luminosity and spectral characteristics of accretion disks. Physically, a higher radiative efficiency implies that a larger portion of the infalling matter's energy is converted into observable radiation, resulting in a more luminous and energetic disk emission. This efficiency is closely related to the Eddington luminosity, which defines the critical threshold at which the outward radiation pressure counterbalances the inward gravitational attraction, setting an upper bound for the stable luminosity of the system. Consequently, elucidating and quantifying the radiative efficiency offer profound insights into the fundamental energy conversion mechanisms governing accretion disk dynamics.

Assuming that all emitted photons can freely propagate to infinity without absorption or scattering, the efficiency ϵ can be expressed in terms of the specific energy of a particle at the marginally stable orbit (r_{isco}).

$$\epsilon = 1 - \tilde{E}_{\text{isco}} \,. \tag{24}$$

In this framework, ϵ reflects the binding energy per unit mass at r_{isco}, thereby linking the disk's radiative properties directly to the underlying spacetime geometry of BH.

Our analysis of the thin accretion disk surrounding PFDM-surrounded Bardeen BH as summarized in Table 1, reveals the distinct influences of the BH's magnetic charge and the surrounding DM parameter on the disk's properties. The radius of the r_{isco} demonstrates a non-monotonic dependence on the PFDM parameter, initially increasing to a maximum around $b/M = 0.9$ before decreasing for higher values, across all considered magnetic charges. Conversely, the radiative efficiency ϵ increases monotonically with b. Furthermore, for a fixed b, a larger g generally results in a smaller r_{isco}, while slightly enhancing the radiative efficiency. These results quantitatively demonstrate that both the PFDM environment and the BH's intrinsic magnetic charge are critical factors governing the accretion flow dynamics and its energy output, with the DM parameter exerting a particularly strong influence on the efficiency of the accretion process.

Table 1. The table illustrates the variation of radiative efficiency ϵ.

g/M	b/M	r_{isco}/M	ϵ
0	0.1	6.88	0.064
	0.5	8.37	0.084
	0.9	9.02	0.101
	1.7	8.78	0.139
0.3	0.1	6.77	0.065
	0.5	8.30	0.089
	0.9	8.95	0.102
	1.7	8.69	0.139
0.5	0.1	6.56	0.066
	0.5	8.16	0.086
	0.9	8.83	0.103
	1.7	8.53	0.141

We now seek to clarify the underlying physical reasons. The term $-\frac{b}{r}\ln\frac{r}{|b|}$ in Equation (6) contributes an additional negative gravitational potential. This effectively superimposes a "shallower" but more extended potential well onto the Schwarzschild or Bardeen potential. Accreting matter falling into this modified potential well releases more gravitational potential energy while moving from larger radii down to the $r_{\rm isco}$. This extra energy is converted into higher radiative flux and luminosity, explaining from an energy conservation perspective why the radiative efficiency $\epsilon = 1 - \tilde{E}_{\rm isco}$ increases with b (as $\tilde{E}_{\rm isco}$ decreases).

5. Conclusions and Discussion

This study employs the Novikov–Thorne model to examine the properties of thin accretion disks of Bardeen BH surrounded by PFDM. The equation determining the ISCO radius is solved numerically to explore the effects of the magnetic charge g and the DM parameter b on the disk's physical characteristics. The analysis reveals that increasing g slightly enhances the energy flux, radiation temperature, luminosity, and radiative efficiency, while causing a minor inward shift of the $\mathrm{r}_{\rm isco}$. In contrast, the DM parameter b exerts a more significant influence, as it shifts the spectral peaks and modifies the overall radiative behavior of the disk.

The results further show that, for the same set of parameters, the PFDM-surrounded Bardeen BH exhibits higher radiation flux and temperature than the PFDM-surrounded Schwarzschild BH. These distinctions imply that while the magnetic charge has a modest effect, the DM parameter plays a dominant role in shaping the disk's observational signatures. As for why the magnetic charge contributes so little to the dynamics, we speculate that several factors may be responsible. From the metric (5), both g and r appear in the denominator. The contribution of g becomes significant only when its magnitude is comparable to r. In the large-scale regions considered in our study, $r \gg g$, so the effect of the magnetic charge on the dynamics is negligible. Its role is only noticeable near the central region, where it serves to remove the curvature singularity inherent in the Bardeen BH, which makes its observational signature extremely difficult to detect. Additionally, the PFDM halo contributes significantly to the overall spacetime geometry. On macroscopic scales, the gravitational influence of DM halo dominates over that of magnetic charge, effectively masking the subtle effects of g in the dynamics. Furthermore, precise observations—such as those from the EHT—could potentially use the parameter b to discriminate between different BH configurations and to probe the influence of DM in strong gravitational environments.

In future research, we plan to further investigate the PFDM-surrounded Bardeen BH by analyzing how the radiation flux generated during accretion disk imaging and jet formation can serve as an observational probe to distinguish it from the predictions of GR. Moreover, we intend to utilize EHT observations to place stringent constraints on the relevant model parameters.

Author Contributions: Formal analysis, D.-D.C.; Investigation, D.-D.C. Writing—original draft, D.-D.C. Writing—review and editing, D.-D.C. and H.F.; Supervision, H.F.; Funding acquisition, H.F. All authors have read and agreed to the published version of the manuscript

Funding: This research was funded by National Natural Science Foundation of China, grant number 12333008.

Data Availability Statement: The original contributions presented in this study are included in the article. Further inquiries can be directed to the corresponding author.

Conflicts of Interest: The authors declare no conflicts of interest.

References

1. Abbott, B.P. et al. [LIGO Scientific Collaboration and Virgo Collaboration]. Observation of Gravitational Waves from a Binary Black Hole Merger. *Phys. Rev. Lett.* **2016**, *116*, 061102. [CrossRef] [PubMed]
2. Abbott, B.P. et al. [LIGO Scientific Collaboration and Virgo Collaboration]. GW150914: The Advanced LIGO Detectors in the Era of First Discoveries. *Phys. Rev. Lett.* **2016**, *116*, 131103. [CrossRef] [PubMed]
3. Akiyama, K. et al. [The Event Horizon Telescope Collaboration]. First M87 Event Horizon Telescope Results. I. The Shadow of the Supermassive Black Hole. *Astrophys. J. Lett.* **2019**, *875*, L1. [CrossRef]
4. Akiyama, K. et al. [The Event Horizon Telescope Collaboration]. First M87 Event Horizon Telescope Results. VI. The Shadow and Mass of the Central Black Hole. *Astrophys. J. Lett.* **2019**, *875*, L6. [CrossRef]
5. Kim, J. First M87 Event Horizon Telescope Results: Array and Instrumentation. In Proceedings of the American Astronomical Society Meeting Abstracts #235, Honolulu, HI, USA, 4–8 January 2020; American Astronomical Society: Washington, DC, USA, 2020; Volume 235, p. 429.04.
6. Akiyama, K. et al. [The Event Horizon Telescope Collaboration]. First M87 Event Horizon Telescope Results. IV. Imaging the Central Supermassive Black Hole. *Astrophys. J. Lett.* **2019**, *875*, L4. [CrossRef]
7. Akiyama, K. et al. [The Event Horizon Telescope Collaboration]. First Sagittarius A* Event Horizon Telescope Results. I. The Shadow of the Supermassive Black Hole in the Center of the Milky Way. *Astrophys. J. Lett.* **2022**, *930*, L12. [CrossRef]
8. Akiyama, K. et al. [The Event Horizon Telescope Collaboration]. First Sagittarius A* Event Horizon Telescope Results. II. EHT and Multiwavelength Observations, Data Processing, and Calibration. *Astrophys. J. Lett.* **2022**, *930*, L13. [CrossRef]
9. Akiyama, K. et al. [The Event Horizon Telescope Collaboration]. First Sagittarius A* Event Horizon Telescope Results. VI. Testing the Black Hole Metric. *Astrophys. J. Lett.* **2022**, *930*, L17. [CrossRef]
10. Akiyama, K. et al. [The Event Horizon Telescope Collaboration]. First Sagittarius A* Event Horizon Telescope Results. IV. Variability, Morphology, and Black Hole Mass. *Astrophys. J. Lett.* **2022**, *930*, L15. [CrossRef]
11. Akiyama, K. et al. [The Event Horizon Telescope Collaboration]. First Sagittarius A* Event Horizon Telescope Results. III. Imaging of the Galactic Center Supermassive Black Hole. *Astrophys. J. Lett.* **2022**, *930*, L14. [CrossRef]
12. Akiyama, K. et al. [The Event Horizon Telescope Collaboration]. First Sagittarius A* Event Horizon Telescope Results. V. Testing Astrophysical Models of the Galactic Center Black Hole. *Astrophys. J. Lett.* **2022**, *930*, L16. [CrossRef]
13. Potapov, A.A.; Garipova, G.M.; Nandi, K.K. Revisiting perfect fluid dark matter: Observational constraints from our galaxy. *Phys. Lett. B* **2016**, *753*, 140–146. [CrossRef]
14. Frank, J.; King, A.; Raine, D.J. *Accretion Power in Astrophysics*, 3rd ed.; Cambridge University Press: Cambridge, UK, 2002.
15. Yuan, F.; Narayan, R. Hot Accretion Flows Around Black Holes. *Annu. Rev. Astron. Astrophys.* **2014**, *52*, 529–588. [CrossRef]
16. Blandford, R.D.; Znajek, R.L. Electromagnetic extraction of energy from Kerr black holes. *Mon. Not. R. Astron. Soc.* **1977**, *179*, 433–456. [CrossRef]
17. Moscibrodzka, M.; Falcke, H.; Shiokawa, H. General relativistic magnetohydrodynamical simulations of the jet in M 87. *Astron. Astrophys.* **2016**, *586*, A38. [CrossRef]
18. Bondi, H. On spherically symmetrical accretion. *Mon. Not. R. Astron. Soc.* **1952**, *112*, 195. [CrossRef]
19. Michel, F.C. Accretion of Matter by Condensed Objects. *Astrophys. Space Sci.* **1972**, *15*, 153–160. [CrossRef]
20. Gralla, S.E.; Holz, D.E.; Wald, R.M. Black Hole Shadows, Photon Rings, and Lensing Rings. *Phys. Rev. D* **2019**, *100*, 024018. [CrossRef]
21. Zeng, X.X.; Zhang, H.Q. Influence of quintessence dark energy on the shadow of black hole. *Eur. Phys. J. C* **2020**, *80*, 1058. [CrossRef]
22. Peng, J.; Guo, M.; Feng, X.H. Influence of quantum correction on black hole shadows, photon rings, and lensing rings. *Chin. Phys. C* **2021**, *45*, 085103. [CrossRef]
23. Zhang, Z.; Hou, Y.; Guo, M. Observational signatures of rotating black holes in the semiclassical gravity with trace anomaly*. *Chin. Phys. C* **2024**, *48*, 085106. [CrossRef]
24. Li, G.P.; He, K.J. Observational appearances of a f(R) global monopole black hole illuminated by various accretions. *Eur. Phys. J. C* **2021**, *81*, 1018. [CrossRef]
25. Zeng, X.X.; Aslam, M.I.; Saleem, R. The optical appearance of charged four-dimensional Gauss–Bonnet black hole with strings cloud and non-commutative geometry surrounded by various accretions profiles. *Eur. Phys. J. C* **2023**, *83*, 129. [CrossRef]
26. Zeng, X.X.; He, K.J.; Li, G.P.; Liang, E.W.; Guo, S. QED and accretion flow models effect on optical appearance of Euler–Heisenberg black holes. *Eur. Phys. J. C* **2022**, *82*, 764. [CrossRef]
27. Meng, Y.; Kuang, X.M.; Wang, X.J.; Wang, B.; Wu, J.P. Images of hairy Reissner–Nordström black hole illuminated by static accretions. *Eur. Phys. J. C* **2024**, *84*, 305. [CrossRef]
28. Wang, K.; Feng, C.J.; Wang, T. Image of Kerr–de Sitter black holes illuminated by equatorial thin accretion disks. *Eur. Phys. J. C* **2024**, *84*, 457. [CrossRef]

29. Feng, H.; Yang, R.J.; Chen, W.Q. Thin accretion disk and shadow of Kerr–Sen black hole in Einstein–Maxwell-dilaton–axion gravity. *Astropart. Phys.* **2025**, *166*, 103075. [CrossRef]
30. Wu, Y.; Feng, H.; Chen, W.Q. Thin accretion disk around black hole in Einstein–Maxwell-scalar theory. *Eur. Phys. J. C* **2024**, *84*, 1075. [CrossRef]
31. Liu, A.; He, T.Y.; Liu, M.; Han, Z.W.; Yang, R.J. Possible signatures of higher dimension in thin accretion disk around brane world black hole. *JCAP* **2024**, *07*, 062. [CrossRef]
32. He, T.Y.; Cai, Z.; Yang, R.J. Thin accretion disks around a black hole in Einstein-Aether-scalar theory. *Eur. Phys. J. C* **2022**, *82*, 1067. [CrossRef]
33. Yin, J.J.; He, T.Y.; Liu, M.; Fan, H.M.; Chen, B.; Han, Z.W.; Yang, R.J. Observational properties of black hole in quantum fluctuation modified gravity. *Nucl. Phys. B* **2025**, *1018*, 117004. [CrossRef]
34. Duque, F.; Sberna, L.; Spiers; A.; Vicente, R. Extreme-mass-ratio inspirals in relativistic accretion discs. *arXiv* **2025**, arXiv:2510.02433.
35. Gjorgjieski, K.; Kunz, J.; Nedkova, P. Comparison of magnetized thick disks around black holes and boson stars. *Eur. Phys. J. C* **2024**, *84*, 286. [CrossRef]
36. Paczyńsky, B.; Wiita, P.J. Thick Accretion Disks and Supercritical Luminosities. *Am. Acad. Pediatr.* **1980**, *88*, 23.
37. Zhang, Z.; Hou, Y.; Guo, M.; Chen, B. Imaging thick accretion disks and jets surrounding black holes. *JCAP* **2024**, *05*, 032. [CrossRef]
38. Bahamonde, S.; Faraji, S.; Hackmann, E.; Pfeifer, C. Thick accretion disk configurations in the Born-Infeld teleparallel gravity. *Phys. Rev. D* **2022**, *106*, 084046. [CrossRef]
39. Zwicky, F. Die Rotverschiebung von extragalaktischen Nebeln. *Helv. Phys. Acta* **1933**, *6*, 110–127.
40. Holmberg, E. A Study of Double and Multiple Galaxies Together with Inquiries into some General Metagalactic Problems. *Ann. Obs. Lund* **1937**, *6*, 1–173.
41. Smith, S. The Mass of the Virgo Cluster. *Astrophys. J.* **1936**, *83*, 23. [CrossRef]
42. Rubin, V.C.; Ford, W.K., Jr.; Thonnard, N. Rotational properties of 21 SC galaxies with a large range of luminosities and radii, from NGC 4605 (R=4kpc) to UGC 2885 (R=122kpc). *Astrophys. J.* **1980**, *238*, 471–487. [CrossRef]
43. Ade, P.A.R. et al. [Planck Collaboration]. Planck 2013 results. XVI. Cosmological parameters. *Astron. Astrophys.* **2014**, *571*, A16. [CrossRef]
44. Barausse, E.; Cardoso, V.; Pani, P. Can environmental effects spoil precision gravitational-wave astrophysics? *Phys. Rev. D* **2014**, *89*, 104059. [CrossRef]
45. Cardoso, V.; Destounis, K.; Duque, F.; Macedo, R.P.; Maselli, A. Black holes in galaxies: Environmental impact on gravitational-wave generation and propagation. *Phys. Rev. D* **2022**, *105*, L061501. [CrossRef]
46. Cheung, M.H.Y.; Destounis, K.; Macedo, R.P.; Berti, E.; Cardoso, V. Destabilizing the Fundamental Mode of Black Holes: The Elephant and the Flea. *Phys. Rev. Lett.* **2022**, *128*, 111103. [CrossRef]
47. Cardoso, V.; Destounis, K.; Duque, F.; Macedo, R.P.; Maselli, A. Gravitational Waves from Extreme-Mass-Ratio Systems in Astrophysical Environments. *Phys. Rev. Lett.* **2022**, *129*, 241103. [CrossRef]
48. Destounis, K.; Kulathingal, A.; Kokkotas, K.D.; Papadopoulos, G.O. Gravitational-wave imprints of compact and galactic-scale environments in extreme-mass-ratio binaries. *Phys. Rev. D* **2023**, *107*, 084027. [CrossRef]
49. Kouniatalis, G.; Suvorov, A.G.; Destounis, K. Lensing by black holes within astrophysical environments. *arXiv* **2025**, arXiv:2508.19333. [CrossRef]
50. Destounis, K.; Fernandes, P.G.S. Chaos and Carter: Extreme-mass-ratio systems of relativistic rotating black holes in astrophysical environments. *arXiv* **2025**, arXiv:2508.20191.
51. Bamber, J.; Clough, K.; Ferreira, P.G.; Hui, L.; Lagos, M. Growth of accretion driven scalar hair around Kerr black holes. *Phys. Rev. D* **2021**, *103*, 044059. [CrossRef]
52. Clough, K.; Ferreira, P.G.; Lagos, M. Growth of massive scalar hair around a Schwarzschild black hole. *Phys. Rev. D* **2019**, *100*, 063014. [CrossRef]
53. Mascher, G.; Destounis, K.; Kokkotas, K.D. Charged black holes in de Sitter space: Superradiant amplification of charged scalar waves and resonant hyperradiation. *Phys. Rev. D* **2022**, *105*, 084052. [CrossRef]
54. Mollicone, A.; Destounis, K. Superradiance of charged black holes embedded in dark matter halos. *Phys. Rev. D* **2025**, *111*, 024017. [CrossRef]
55. Fernandes, P.G.S.; Cardoso, V. Spinning Black Holes in Astrophysical Environments. *Phys. Rev. Lett.* **2025**, *135*, 211403. [CrossRef] [PubMed]
56. Pezzella, L.; Destounis, K.; Maselli, A.; Cardoso, V. Quasinormal modes of black holes embedded in halos of matter. *Phys. Rev. D* **2025**, *111*, 064026. [CrossRef]
57. Courty, A.; Destounis, K.; Pani, P. Spectral instability of quasinormal modes and strong cosmic censorship. *Phys. Rev. D* **2023**, *108*, 104027. [CrossRef]

58. Destounis, K.; Malato Corrêa, M.; Macedo, C.F.B.; Panosso Macedo, R. Spectral instability of horizonless compact objects within astrophysical environments: The "exotic" elephant and the flea. *arXiv* **2025**, arXiv:2509.16310. [CrossRef]
59. Rahaman, F.; Nandi, K.K.; Bhadra, A.; Kalam, M.; Chakraborty, K. Perfect Fluid Dark Matter. *Phys. Lett. B* **2011**, *694*, 10–15. [CrossRef]
60. Kiselev, V.V. Quintessential solution of dark matter rotation curves and its simulation by extra dimensions. *arXiv* **2003**, arXiv:gr-qc/0303031. [CrossRef]
61. Kiselev, V.V. Vector field as a quintessence partner. *Class. Quant. Grav.* **2004**, *21*, 3323–3336. [CrossRef]
62. Kiselev, V.V. Vector field and rotational curves in dark galactic halos. *Class. Quant. Grav.* **2005**, *22*, 541–558. [CrossRef]
63. Li, M.H.; Yang, K.C. Galactic Dark Matter in the Phantom Field. *Phys. Rev. D* **2012**, *86*, 123015. [CrossRef]
64. Jusufi, K.; Jamil, M.; Salucci, P.; Zhu, T.; Haroon, S. Black hole surrounded by a dark matter halo in the M87 galactic center and its identification with shadow images. *Phys. Rev. D* **2019**, *100*, 044012. [CrossRef]
65. Borde, A. Regular black holes and topology change. *Phys. Rev. D* **1997**, *55*, 7615–7617. [CrossRef]
66. Bardeen, J. Non-singular general relativistic gravitational collapse. In Proceedings of the 5th International Conference on Gravitation and the Theory of Relativity, Tbilisi, Georgia, 9–16 September 1968; p. 87.
67. Ayon-Beato, E.; Garcia, A. The Bardeen model as a nonlinear magnetic monopole. *Phys. Lett. B* **2000**, *493*, 149–152. [CrossRef]
68. Zhang, H.X.; Chen, Y.; Ma, T.C.; He, P.Z.; Deng, J.B. Bardeen black hole surrounded by perfect fluid dark matter. *Chin. Phys. C* **2021**, *45*, 055103. [CrossRef]
69. Kiselev, V.V. Quintessence and black holes. *Class. Quant. Grav.* **2003**, *20*, 1187–1198. [CrossRef]
70. Gnedin, O. Y.; Primack, J. R. Dark Matter Profile in the Galactic Center. *Phys. Rev. Lett.* **2004**, *93*, 061302. [CrossRef]
71. Kovacs, Z.; Harko, T. Can accretion disk properties observationally distinguish black holes from naked singularities? *Phys. Rev. D* **2010**, *82*, 124047. [CrossRef]
72. Gair, J.R.; Li, C.; Mandel, I. Observable Properties of Orbits in Exact Bumpy Spacetimes. *Phys. Rev. D* **2008**, *77*, 024035. [CrossRef]
73. Bambi, C.; Barausse, E. Constraining the quadrupole moment of stellar-mass black-hole candidates with the continuum fitting method. *Astrophys. J.* **2011**, *731*, 121. [CrossRef]
74. Bambi, C.; Barausse, E. The Final stages of accretion onto non-Kerr compact objects. *Phys. Rev. D* **2011**, *84*, 084034. [CrossRef]
75. Shakura, N.I.; Sunyaev, R.A. Black holes in binary systems. Observational appearance. *Astron. Astrophys.* **1973**, *24*, 337–355.
76. Novikov, I.D.; Thorne, K.S. Astrophysics and Black Holes. In *Proceedings of the Les Houches Summer School of Theoretical Physics: Black Holes*; DeWitt, B.S., Ed.; Gordon and Breach: New York, NY, USA; Les Houches: Haute-Savoie, France, 1972; pp. 343–550.
77. Thorne, K.S. Disk accretion onto a black hole. 2. Evolution of the hole. *Astrophys. J.* **1974**, *191*, 507–520. [CrossRef]
78. Page, D.N.; Thorne, K.S. Disk-Accretion onto a Black Hole. Time-Averaged Structure of Accretion Disk. *Astrophys. J.* **1974**, *191*, 499–506. [CrossRef]
79. Collodel, L.G.; Doneva, D.D.; Yazadjiev, S.S. Circular Orbit Structure and Thin Accretion Disks around Kerr Black Holes with Scalar Hair. *Astrophys. J.* **2021**, *910*, 52. [CrossRef]
80. Torres, D.F. Accretion disc onto a static nonbaryonic compact object. *Nucl. Phys. B* **2002**, *626*, 377–394. [CrossRef]
81. Banerjee, I.; Mandal, B.; SenGupta, S. Implications of Einstein–Maxwell dilaton–axion gravity from the black hole continuum spectrum. *Mon. Not. R. Astron. Soc.* **2020**, *500*, 481–492. [CrossRef]
82. Bhattacharyya, S.; Misra, R.; Thampan, A.V. General relativistic spectra of accretion disks around rotating neutron stars. *Astrophys. J.* **2001**, *550*, 841. [CrossRef]
83. Luminet, J.P. Image of a spherical black hole with thin accretion disk. *Astron. Astrophys.* **1979**, *75*, 228–235.

https://doi.org/10.3390/universe12010008